


Screening of thermoelectric silicides with atomistic transport calculations


Cite as: J. Appl. Phys. **128**, 125105 (2020); <https://doi.org/10.1063/5.0008198>

Submitted: 20 March 2020 . Accepted: 17 August 2020 . Published Online: 23 September 2020

 Ole Martin Løvrik, Espen Flage-Larsen, and Gunstein Skomedal

COLLECTIONS

 This paper was selected as Featured

 This paper was selected as Scilight



View Online



Export Citation



CrossMark

ARTICLES YOU MAY BE INTERESTED IN

[Screening more than 1,500 silicides to determine their thermoelectric properties](#)
Scilight **2020**, 391107 (2020); <https://doi.org/10.1063/10.0002131>

[Photothermal testing of composite materials: Virtual wave concept with prior information for parameter estimation and image reconstruction](#)

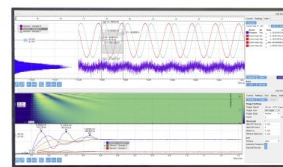
Journal of Applied Physics **128**, 125108 (2020); <https://doi.org/10.1063/5.0016364>

[Phonon properties and thermal conductivity from first principles, lattice dynamics, and the Boltzmann transport equation](#)

Journal of Applied Physics **125**, 011101 (2019); <https://doi.org/10.1063/1.5064602>

Challenge us.

What are your needs for
periodic signal detection?



Zurich
Instruments

Screening of thermoelectric silicides with atomistic transport calculations



Cite as: J. Appl. Phys. 128, 125105 (2020); doi: 10.1063/5.0008198

Submitted: 20 March 2020 · Accepted: 17 August 2020 ·

Published Online: 23 September 2020



Ole Martin Løvrik,^{1,a)}  Espen Flage-Larsen,¹ and Gunstein Skomedal²

AFFILIATIONS

¹SINTEF Materials Physics, NO-0314 Oslo, Norway

²Elkem ASA, NO-4675 Kristiansand, Norway

^{a)}Author to whom correspondence should be addressed: ole.martin.lowik@sintef.no

ABSTRACT

More than 1000 crystalline silicide materials have been screened for thermoelectric properties using first-principles atomistic calculations coupled with the semi-classical Boltzmann transport equation. Compounds that contain radioactive, toxic, rare, and expensive elements as well as oxides, hydrides, carbides, nitrides, and halides have been neglected in the study. The already well-known silicides with good thermoelectric properties, such as SiGe, Mg₂Si, and MnSi_x, are successfully predicted to be promising compounds along with a number of other binary and ternary silicide compositions. Some of these materials have only been scarcely studied in the literature, with no thermoelectric properties being reported in experimental papers. These novel materials can be very interesting for thermoelectric applications provided that they can be heavily doped to give a sufficiently high charge carrier concentration and that they can be alloyed with isoelectronic elements to achieve adequately low phonon thermal conductivity. The study concludes with a list of the most promising silicide compounds that are recommended for further experimental and theoretical investigations.

© 2020 Author(s). All article content, except where otherwise noted, is licensed under a Creative Commons Attribution (CC BY) license (<http://creativecommons.org/licenses/by/4.0/>). <https://doi.org/10.1063/5.0008198>

I. INTRODUCTION

Thermoelectric (TE) devices can be used for a variety of purposes,^{1,2} and their potential as solid-state heat engines converting low-quality heat into electricity has lately received much attention.³ Much of the focus has been on optimizing the TE figure of merit,

$$ZT = \frac{\alpha^2 \sigma}{(\kappa_{\text{el}} + \kappa_{\text{ph}})} T,$$

where T is the temperature, α is the Seebeck coefficient, σ is the electrical conductivity, and κ_{el} (κ_{ph}) is the electron (phonon) contribution to the thermal conductivity κ .^{4–6}

Another important challenge is to replace the TE materials used in present commercial TE generators, since they are based on toxic and scarce elements such as Bi, Te, and Pb.^{7,8} A promising group of alternative materials are silicides, based on silicon which is abundant and non-toxic. A number of silicides have been investigated as potential TE materials in the literature, and a recent review listed the TE properties of 20–30 different silicide compositions.⁹

Almost all these are binary silicides, with Mg₂Si, MnSi_x, and Si–Ge being the most prominent examples. In the cases where more than two elements are present, a solid solution of two isoelectronic elements usually replaces one element, as in the case of Mg₂(Si,Sn). This is isoelectronic to the base compound (Mg₂Si), and there are two main effects of adding the third element. One is to reduce the phonon thermal conductivity by alloy scattering on the solid solution sublattice (the Si,Sn sublattice), thus enhancing the TE figure of merit ZT .¹⁰ The other is to optimize the band structure by aligning bands contributing to the TE transport, i.e., to increase the band degeneracy and consequently the power factor.¹¹ So far, a few experimental efforts have identified promising TE materials based on silicides that are truly ternary, i.e., consisting of three chemically different elements. None of these studies have optimized the materials extensively, which means that their true TE potential may not yet have been revealed. An important task of the present study will thus be to investigate the TE potential of both binary and ternary silicides with theoretical modeling based on first-principles (FP).

Predicting ZT from FP is a challenging task. The traditional way is to treat the TE electronic properties with the Boltzmann

transport equation (BTE) within the electron relaxation time approximation (RTA), using the electronic band structure from density functional theory (DFT) calculations as input. Several assumptions and approximations are necessary,^{5,12,13} and it is often difficult to compare results from modeling with experimental studies.¹⁴ Nevertheless, recent development of theory and models has led to the significantly improved quality of FP-based predictions. New numerical techniques have made it possible to describe the electronic band structure in a highly efficient manner,^{15–17} e.g., making it feasible to use high-level theoretical techniques like hybrid functionals with the exact Fock exchange to calculate TE properties.¹⁶ New methods have made it possible to add electron–phonon interaction to predict the electron relaxation time from first-principles calculations, which is necessary for the electronic parts of the figure of merit (α , σ , and κ_{el}).^{12,18,19} Recently developed techniques can similarly be used to predict lattice thermal conductivity from first-principles calculations.^{20,21} In some materials, the predicted TE properties including ZT are now very close to experimental values.^{13,22}

At the same time, the rapid growth of computational resources has made it possible to perform FP simulations of many different compounds in a single study. A number of recent papers have thus reported high-throughput screening studies searching for TE materials using FP calculations.^{11,23–30} As an example, the pioneering work of Madsen²⁶ investigated 570 compounds containing Sb, using a constant relaxation time (CRT) and constant κ_{ph} as implemented in the BoltzTraP code.³¹ A similar technique was used to explore the TE properties of more than 48 000 inorganic compounds from the Materials Project database.³²

We have used the Transport for Materials (T4ME) approach in this work, which is a new implementation of BTE that exploits newly developed internal interpolation routines in the Vienna *ab initio* simulation package (VASP)^{33,34} to efficiently obtain the very high density of integration points in reciprocal space that is necessary to obtain proper convergence of the transport properties.³⁵ This opens up the possibility to work at a theoretical level higher than the usual DFT used in screening studies. This tool also has a number of scattering properties integrated, making it possible to investigate the effect of different scattering mechanisms on the electronic transport properties. As a demonstration of the method's versatility, it has in the present paper been used to perform high-accuracy screening of more than 1000 silicide systems for TE properties, based on DFT calculations based on BTE. A constant relaxation time (corresponding to scattering from neutral impurities) and constant κ_{ph} were used for the majority of the materials to reduce the computational cost. In a final, high-accuracy step, the electron relaxation time was calculated with acoustic phonon (AP) scattering by the deformation potential method, and the phonon thermal conductivity was calculated with the temperature-dependent effective potential (TDEP) method.²⁰ This was only performed on a small list of promising materials. The paper concludes with a list of the most promising silicides for TE applications.

II. METHODOLOGY

A. Pre-screening

The screening was based on all listed binary and ternary materials containing silicon in the MaterialsProject (MP) database.³⁶ The MP database has been produced using DFT calculations with

VASP. This makes MP a very useful database for our purpose, since the crystal structures are already structurally relaxed at a theoretical level close to ours. It contained 8605 silicides at the time of search (November 2019). These are all unique; no two entries have the same composition and crystal structure. The MP database contains on the other hand a number of unstable and hypothetical materials, which may or may not be possible to synthesize.

The screening was performed in several steps, as shown in Fig. 1. Before assessing the TE properties, the following groups of materials were excluded:

- Oxides, hydrides, carbides, nitrides, and halides.
- Toxic elements. This was based on the *Restriction of Hazardous Substances Directive*,³⁷ avoiding Pb, Hg, and Cd.
- Radioactive elements, thus excluding U, Pm, Ac, Th, Pa, Np, and Pu.
- Rare elements. The abundance of elements was taken from Ref. 38, and the threshold abundance in the Earth's crust was selected as 0.004 pm. This excluded Os, Ru, Rh, Ir, and Te.
- Expensive elements. The price of the elements was taken from Ref. 39, and the threshold was selected to be 12 000 USD/kg. The excluded elements from this criterion were Rb, Sc, Yb, Cs, Tm, Lu, Pd, Pt, and Au.
- Thermodynamically unstable compounds. Compounds with a listed formation energy in MP higher than 0.15 eV were excluded. The formation energy is defined as the energy of the compound compared to that of the constituting elements.
- Chemically unstable compounds. Compounds with a listed energy above hull in MP higher than 0.16 eV were excluded. The energy above hull is defined as the energy of the compound compared to that of the most stable linear combination of competing compounds.
- Compounds with large bandgap. Compounds with a listed the bandgap in MP higher than 1.0 eV were excluded. The bandgaps in MP have been calculated at the generalized gradient approximation (GGA) level and are thus likely to be underestimated.

The result of these pre-screening steps was that the number of systems to be studied with high-throughput transport calculations was reduced from 8605 to 1559.

B. Transport calculations

The next step in the screening procedure was to estimate the potential TE efficiency of the remaining materials, using transport calculations based on FP. Two steps were employed to this end: a high-throughput screening of all the remaining systems selected a small number of promising systems, which were further investigated with higher precision.

The transport equations were based on the electronic structure generated with density functional theory (DFT) computations at the generalized gradient approximation (GGA) level, using the Perdew, Burke, and Ernzerhof (PBE) functional.⁴⁰ We used the Vienna *ab initio* simulation package (VASP),^{33,34} which is a plane wave code employing the projector augmented wave (PAW) method to treat the core regions.⁴¹

The electronic structure from the DFT calculations was used as the input to the semi-classical Boltzmann transport equation

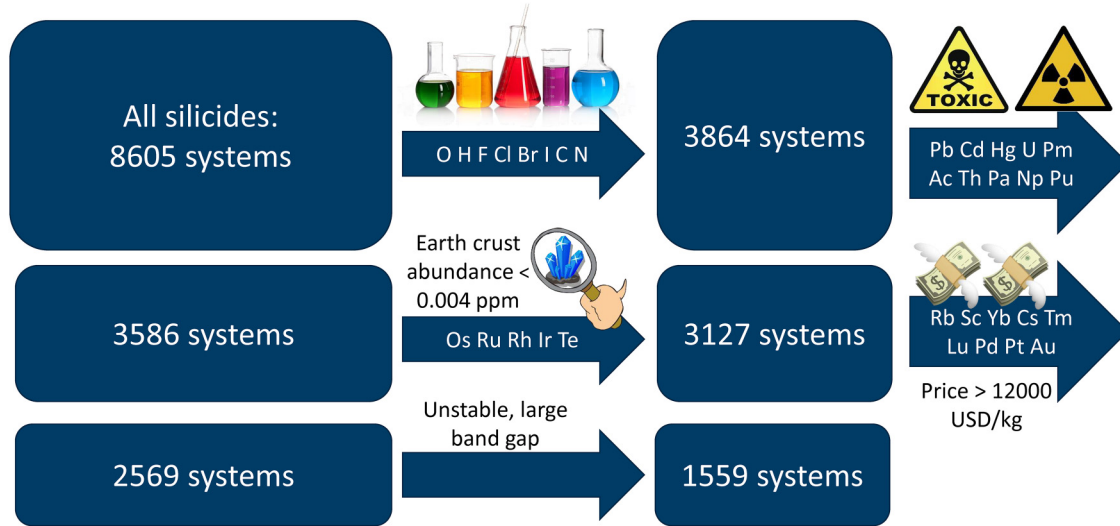


FIG. 1. The first steps of the silicide screening based on the MaterialsProject database.³⁶ The pre-screening consisted of excluding unwanted chemistry (oxides, hydrides, carbides, nitrides, and halides) in addition to toxic, radioactive, rare, and expensive elements. 2569 systems remained after these steps. Additionally, thermodynamically and chemically unstable compounds (see the main text for definitions of this) were excluded, as well as materials with a GGA-calculated bandgap >1.0 eV. This brought the number of input systems down to 1559. Those systems were used as input to the high-throughput screening using first-principles transport calculations.

(BTE) using the relaxation time approximation (RTA).^{4,42} A new implementation of the BTE was employed: the Transport for Materials (T4ME) approach.¹⁷ This has a number of advantages, including a very efficient interpolation scheme coupled to internal interpolation of \mathbf{k} -points in VASP. This makes high-throughput, high-accuracy transport calculations more viable.

The BTE calculations made use of the DFT-calculated electronic band structure $\epsilon_n(\mathbf{k})$, where the energy ϵ of band n depends on the wave vector \mathbf{k} . The electrical conductivity tensor σ_{ij} can then be calculated as follows:

$$\sigma_{ij} = \frac{e^2}{V} \sum_n \int \tau_n(\mathbf{k}) \left(-\frac{\partial f_n(\mathbf{k})}{\partial \epsilon} \right) v_i^n v_j^n d\mathbf{k},$$

where e is the elementary charge, V is the crystal volume, τ is the electron scattering time within the RTA, f is the Fermi-Dirac distribution function, and v_i^n is the Fermi velocity. The latter can be obtained from the band structure by

$$v_i^n = \frac{1}{\hbar} \nabla_{k_i} \epsilon_n(\mathbf{k}).$$

By using the χ tensor,

$$\chi_{ij} = \frac{e}{TV} \sum_n \int \tau_n(\mathbf{k}) (\epsilon_n(\mathbf{k}) - \mu) \left(-\frac{\partial f_n(\mathbf{k})}{\partial \epsilon} \right) v_i^n v_j^n d\mathbf{k},$$

the Seebeck coefficient is given by

$$\alpha_{kl} = (\sigma^{-1})_{ki} \chi_{il}.$$

The integrals are converted into energy-dependent ones on the following form:

$$\sigma_{ij} = e^2 \sum_n \int \sum_{ij}^{0,n}(\epsilon) \left(-\frac{\partial f_n(\mathbf{k})}{\partial \epsilon} \right) d\epsilon,$$

where

$$\sum_{ij}^{p,n}(\epsilon) = \frac{1}{n_k} \sum_k \tau_n(\epsilon) (\epsilon_n(\mathbf{k}) - \mu)^p v_i^n v_j^n \delta(\epsilon - \epsilon_n(\mathbf{k})).$$

The χ tensor then takes the following form:

$$\chi_{ij} = \frac{e}{TV} \int \sum_{ij}^{1,n}(\epsilon) \left(-\frac{\partial f_n(\mathbf{k})}{\partial \epsilon} \right) d\epsilon,$$

and the electronic part of the thermal conductivity κ_{el} is given by

$$\kappa_{ij}^{el} = \kappa_{ij}^0 - T \chi_{ik} \chi_{kj},$$

where

$$\kappa_{ij}^0 = \frac{1}{e^2 T} \int \sum_{ij}^{2,n}(\epsilon) \left(-\frac{\partial f_n(\mathbf{k})}{\partial \epsilon} \right) d\epsilon.$$

The Lorenz function L is defined as the relationship between σ and κ_{el} through the Wiedemann-Franz law,

$$L = \frac{\kappa_{el}}{\sigma T}.$$

A constant relaxation time (CRT) $\tau = \tau_0$ was used within the RTA for the high-throughput part of the screening, using $\tau_0 = 10^{-13}$ s. This is in line with several previous screening studies (e.g., Refs. 23 and 26). It is relatively optimistic, assuming that contributions from impurity and acoustic phonon scattering are moderate. Also, τ_0 is known to be temperature dependent, and we can expect it to be lower at higher temperature due to increased scattering. Thus, the results presented at high temperature (800 K) below can be expected to exaggerate the TE figure of merit.

To allow for a simplified treatment of electron scattering and phonon thermal conductivity, we initially focused on two temperatures during the screening: 300 and 800 K. This represents the two most important application areas of TE devices: room temperature applications and high-temperature waste heat harvesting.

The lattice part of the thermal conductivity κ_{ph} was selected to be fixed at $1.9 \text{ W m}^{-1} \text{ K}^{-1}$ at 300 K and $1.4 \text{ W m}^{-1} \text{ K}^{-1}$ at 800 K during the high-throughput screening, similar to the lowest values that have been obtained experimentally for compounds based on Mg_2Si .⁹ These are optimistic values assuming that it is possible to nanostructure the sample and also to reduce phonon scattering by alloying on at least one sublattice [which, e.g., is one of the reasons $\text{Mg}_2(\text{Sn},\text{Si})$ has significantly lower κ_{ph} than Mg_2Si ¹⁰].

In the final, high-accuracy calculations, electron–phonon coupling was included by using the deformation potential method;^{43,44} this was used to predict the electron relaxation time from acoustic phonon (AP) scattering in the final, high-accuracy step. The AP electron relaxation time is given by⁴⁴

$$\frac{1}{\tau^{\text{AP}}(\epsilon)} = \frac{\sqrt{2}m^{3/2}k_BTE_1^2}{\pi\hbar^4\rho v_l^2}\epsilon^{1/2},$$

where m is the effective mass, k_B is the Boltzmann constant, E_1 is the deformation potential constant, ρ is the density, and v_l is the longitudinal sound velocity. E_1 was found by calculating the variation of the valence band maximum as a function of the lattice deformation, keeping the 1s orbital as a reference energy.⁴⁵ The longitudinal sound velocity,

$$v_l = \sqrt{\frac{B + \frac{4}{3}G}{\rho}},$$

was extracted from the bulk (B) and shear (G) moduli, which, in turn, were calculated from the elastic constants generated from the stress–strain relationships resulting from distortions of the lattice from equilibrium.⁴⁶ This can be rewritten to define the acoustic phonon scattering prefactor time τ_0^{AP} ,

$$\tau^{\text{AP}}(\epsilon) = \frac{\pi\hbar^4\rho v_l^2}{\sqrt{2}(mk_B T)^{3/2}E_1^2}\sqrt{\frac{k_B T}{\epsilon}} \equiv \tau_0^{\text{AP}}\sqrt{\frac{k_B T}{\epsilon}}.$$

The phonon thermal conductivity κ_{ph} was also calculated in the final step, using the TDEP method.²⁰ The diagonal components

in Cartesian direction i were then found from

$$\kappa_{ii}^{\text{ph}} = \frac{1}{V} \sum_{\mathbf{q}s} C_{\mathbf{q}s} v_{\mathbf{q}s}^2 \tau_{\mathbf{q}s},$$

where

$$C_{\mathbf{q}s} = \hbar\omega_{\mathbf{q}s} \frac{\partial n_{\mathbf{q}s}^0}{\partial T}$$

is the specific heat of the phonon mode with wave vector \mathbf{q} and branch index s , $v_{\mathbf{q}s}$ is the phonon velocity, and $\tau_{\mathbf{q}s}$ is the phonon lifetime. Here, $\omega_{\mathbf{q}s}$ is the phonon frequency and $n_{\mathbf{q}s}^0$ is the Bose–Einstein distribution function. The phonon lifetimes were found by an iterative solution of the phonon Boltzmann transport equation, using second- and third-order force constants extracted from *ab initio* molecular dynamics calculations with temperature-dependent anharmonic effective potentials.⁴⁷

The doping level was optimized in all these calculations by using the electronic chemical potential as a free parameter; this assumes that the optimal doping level (which might be very high in some cases) is available in experiments. This gave a predicted figure of merit ZT_0 that describes an upper, theoretical limit of the experimentally achievable figure of merit ZT . We can thus expect false positives from this screening procedure, predictions of promising TE materials that turn out to be poor from experiments. The number of false negatives should be minimized for the same reason, with one important exception: the cases where GGA predicts a very small or missing bandgap, where the material in reality is a small bandgap semiconductor or a half-metal. To avoid this would require significantly more expensive methods and was thus excluded in the present study.

III. RESULTS AND DISCUSSION

A. Magnesium silicide

An example of the results for one specific compound is shown for Mg_2Si at $T = 300$ and 800 K in Fig. 2. Two different values of the constant relaxation time τ_0 are selected: $\tau_0 = 10^{-13}$ s and 10^{-14} s. It is there shown how the various transport properties vary as a function of the chemical potential μ , i.e., the position of the Fermi level relative to the valence band edge. It is demonstrated in Figs. 2(a) and 2(b) how the material changes from p-doped (positive Seebeck coefficient and $p > n$) to n-doped at $\mu \cong 0.03 - 0.05$ eV, depending on temperature. The charge carrier concentration [Fig. 2(b)] is in the order of 10^{20} cm^{-3} when the material has peak performance (around ± 0.1 eV); the electrical conductivity [Fig. 2(c)] is in the same region in the order of $10^5 - 10^6 \text{ S m}^{-1}$, while the electronic part of the thermal conductivity [Fig. 2(d)] varies significantly (between 0.1 and more than $10 \text{ W m}^{-1} \text{ K}^{-1}$) in the same region, depending on the temperature and τ . The figure of merit [Fig. 2(e)] indicates that Mg_2Si in theory can be both a good n-doped (ZT_0 up to 1.6 for $\mu \cong -0.09$ eV at 300 K) and p-doped (ZT_0 up to 0.7 for $\mu \cong 0.14$ eV at 300 K) TE material. It can further be seen from Fig. 2(f) that the Lorenz number varies quite dramatically around $\mu = 0$, as expected due to bipolar contributions.^{48,49} However, it displays reasonable values

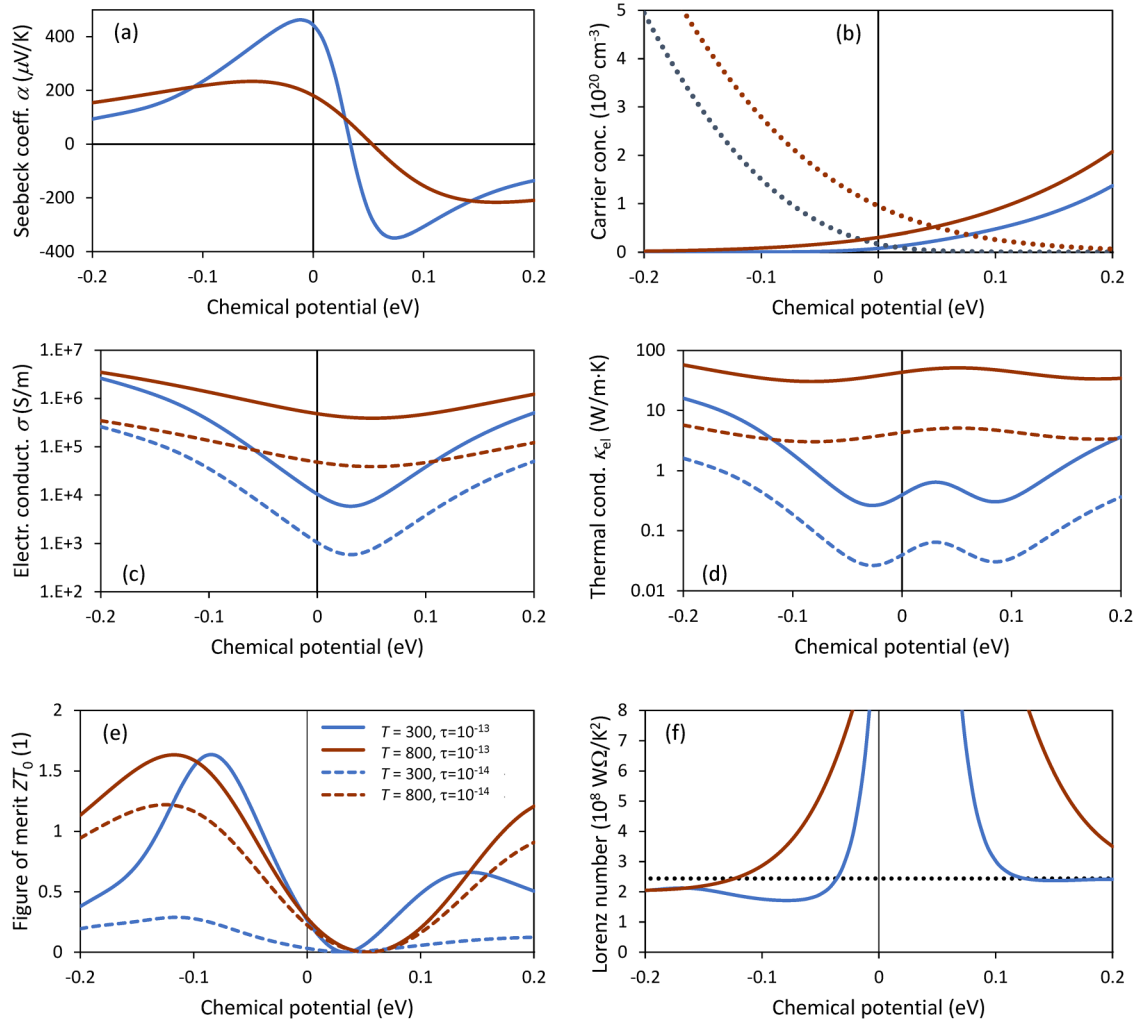


FIG. 2. The thermoelectric properties of Mg₂Si at $T = 300$ K (blue curves) and 800 K (red curves) as a function of the chemical potential, based on a constant relaxation time (CRT) of $\tau_0 = 10^{-13}$ s (solid curves) and 10^{-14} s (dashed curves): the Seebeck coefficient α (a), the n (solid lines) and p (dotted lines) charge carrier concentration (b), the electrical conductivity σ (c), the electrical part of the thermal conductivity κ_{el} (d), the predicted dimensionless figure of merit ZT_0 (e), and the Lorenz number (f)—the dotted, horizontal line designates the Sommerfeld value $L_0 = 2.44 \times 10^8 \text{ W}\Omega/\text{K}^2$.

between 1.7 and $2.4 \times 10^8 \text{ W}\Omega/\text{K}^2$ in the regions with high TE performance, as shown by the dotted line representing the theoretical Sommerfeld value $L_0 = 2.44 \times 10^8 \text{ W}\Omega/\text{K}^2$.

The predicted phonon thermal conductivity κ_{ph} of Mg₂Si is shown as a function of temperature in Fig. 3. Three different phonon scattering mechanisms were successively added in the calculations: anharmonic three-phonon scattering, alloy scattering with 25% Sn at the Si site (using isotope scattering and the virtual crystal approximation to include the effect of alloying),⁵⁰ and grain boundary (GB) scattering with a grain size of 50 nm. The latter mechanism assumes that all phonons with a mean free path larger than the grain size will be scattered.⁵⁰ The values due to only anharmonic scattering are relatively high, and it is clear that adding

alloy scattering is crucial to bring down κ_{ph} to acceptable values for TE applications. Adding grain boundary scattering on top of this yields values that are excellent, below $1 \text{ W m}^{-1} \text{ K}^{-1}$.

We next investigate how the final, high-accuracy step influences the results of Mg₂Si—this includes implementing deformation potential based acoustic phonon scattering in addition to first-principles phonon thermal conductivity from TDEP. The results of this are shown for n-doped Mg₂Si in Fig. 4 and compared to experimental results for three different systems: “Mg₂Si,”⁵¹ “Mg₂Si_{0.95}Ge_{0.05},”⁵² and “Mg₂Si_{0.3}Sn_{0.7}.”⁵³ The “Mg₂Si” system was n-doped with 2% Al, and 0.25% glass frit was added to enhance the mechanical properties.⁵¹ This material was sufficiently doped to achieve reasonable values of σ and κ , but the figure of merit was

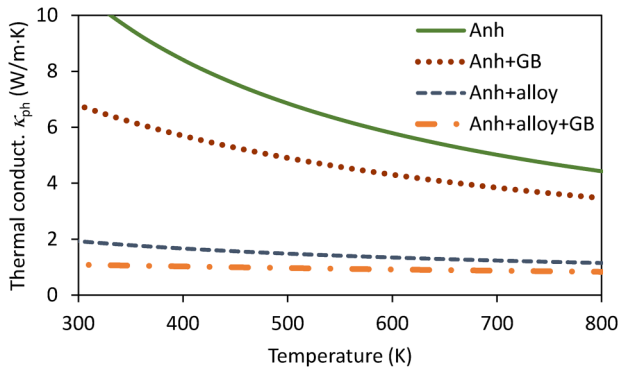


FIG. 3. The calculated phonon thermal conductivity κ_{ph} of Mg_2Si with combinations of three different phonon scattering regimes: Anharmonic (Anh) three-phonon scattering (green, solid curve), alloy scattering based on 25% Sn on the Si site added to Anh (gray, dashed curve), grain boundary (GB) scattering with a typical grain size of 50 nm added to Anh (red, dotted curve), and a combination of all three mechanisms (orange, dashed-dotted curve).

barely passing 0.5 around $T = 800$ K. The “ $\text{Mg}_2\text{Si}_{0.95}\text{Ge}_{0.05}$ ” system was n-doped with 0.23% Sb, giving a nominal carrier concentration of $0.33 \times 10^{20} \text{ cm}^{-3}$ and features like a heavily doped semiconductor (e.g., decreasing σ with T).⁵² The “ $\text{Mg}_2\text{Si}_{0.3}\text{Sn}_{0.7}$ ” system is one of

the best reported Mg_2Si -based materials in the literature, with a peak ZT around 1.33 at 700 K; this was n-doped with 0.6% Sb, giving a charge carrier concentration of $1.7 \times 10^{20} \text{ cm}^{-3}$.⁵³

The correspondence between the predicted properties and experimental values gives important clues about the active scattering mechanisms in the real samples. Starting with the Seebeck coefficient α , it appears that the CRT scattering with $\tau_0 = 10^{-14}$ s and $n = 2.6 \times 10^{20} \text{ cm}^{-3}$ is the predicted curve that follows the experimental ones most closely, with only slightly too low absolute values of α . This indicates that neutral impurities may play an important role in the electron scattering of these systems.

Turning to the electrical conductivity, however, the temperature behavior of the experiments (decreasing σ with T) is not very well described by the CRT mechanism, as σ increases with T like in a regular semiconductor. This is slightly less so in the case of acoustic phonon (AP) scattering, where σ decreases slightly with T before increasing at higher temperatures. The experimental decrease is probably due to the impurity bands responsible for the charge carrier concentration at low temperature being emptied as the temperature increases. This is not accounted for by any of the scattering models of the present study, which rely on the rigid band approximation. Also, the theoretical predictions rely on a bandgap that is too low, leading to significant contributions from minority carriers at the highest temperatures in Fig. 4. Nevertheless, it is

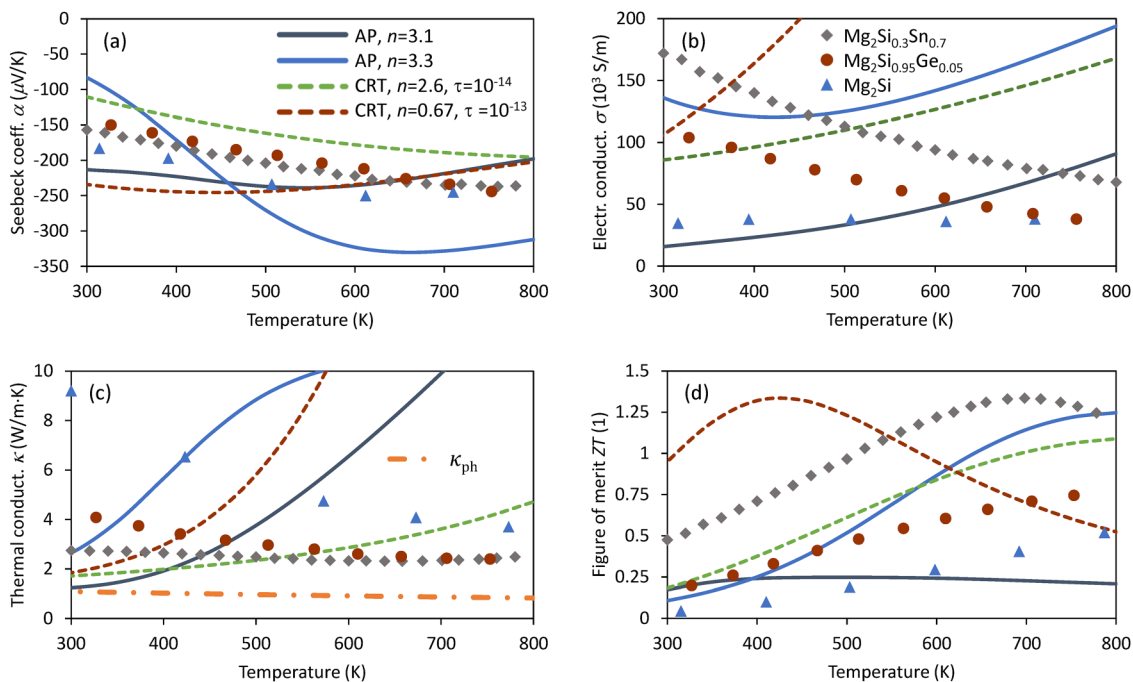


FIG. 4. The thermoelectric properties of n-doped Mg_2Si calculated using a constant relaxation time (CRT) with $\tau_0 = 10^{-13}$ s and a charge carrier concentration of $n = 0.67 \times 10^{20} \text{ cm}^{-3}$ (red dashed curves); CRT with $\tau_0 = 10^{-14}$ s and $n = 2.6 \times 10^{20} \text{ cm}^{-3}$ (green dashed curves); acoustic phonon (AP) scattering with $n = 3.3 \times 10^{20} \text{ cm}^{-3}$ (blue solid curves); and AP with $n = 3.1 \times 10^{20} \text{ cm}^{-3}$ (gray solid curves). The predicted values are compared with experimental data of Mg_2Si (Ref. 51, blue triangles), $\text{Mg}_2\text{Si}_{0.95}\text{Ge}_{0.05}$ (Ref. 52, red circles), and $\text{Mg}_2\text{Si}_{0.3}\text{Sn}_{0.7}$ (Ref. 53, gray diamonds). The panels display the Seebeck coefficient α (a), the electrical conductivity σ (b), the thermal conductivity κ including the calculated lattice part κ_{ph} as the dashed-dotted orange curve (c), and the dimensionless figure of merit ZT_0 (d).

worth noting that even though σ from AP scattering was predicted without any other adjustable parameters than the charge carrier concentration, the correspondence with the “Mg₂Si” system is quite good, both qualitatively and quantitatively. This indicates that AP scattering is a relevant mechanism particularly in the case without alloy substitution on the Si site.

The same type of discrepancy between experiment and theory can be seen for the thermal conductivity κ . While the calculated phonon part κ_{ph} decreases as a function of temperature, an opposite and stronger trend is seen for the electronic part κ_{el} , which results in an overall increasing behavior. The experimental trend is as expected from the Wiedemann–Franz law, combined with a weakly decreasing κ_{ph} .

When the transport parameters are combined in the figure of merit, the different scattering regimes behave surprisingly well compared to the experimental data. This is partially because discrepancies in σ and κ_{el} are canceled due to the Wiedemann–Franz law. The largest qualitative deviation between experiment and theory is found for the CRT scattering with $n = 0.67 \times 10^{20} \text{ cm}^{-3}$ and $\tau_0 = 10^{-13} \text{ s}$. The charge carrier concentration was optimized for low temperatures in this case, which means that the performance at high temperature is poor compared to that at room temperature.

The best n-doped Mg₂Si systems are thus quite well described by the techniques of the present paper. To obtain optimal doping concentrations for p-doped Mg₂Si is more challenging experimentally, since Mg₂Si is intrinsically n-doped.⁵⁴ Nevertheless, it has been shown that a p-doping concentration of around 10^{20} cm^{-3} is optimal at $T = 700 \text{ K}$,⁵⁵ which is very similar to what was found in the present paper [Fig. 2(b) at $\mu \sim -0.1 \text{ eV}$]. This can be achieved with Li-doping,⁵⁶ but the optimally doped samples display significantly lower values at 300 K for the Seebeck coefficient ($\sim 100 \mu\text{V K}^{-1}$), electrical conductivity ($\sim 5 \times 10^{-4} \text{ S m}^{-1}$), and figure of merit (~ 0.1) than is predicted in Fig. 2. This can partially be explained by precipitates (micrometer-sized MgO⁵⁶). However, the heavily doped samples also experience a drop in mobility,⁵⁶ which may point to a reduced lifetime of charge carriers due to increased impurity scattering. In other words, the choice of $\tau_0 = 10^{-13} \text{ s}$ may be too optimistic when very high doping levels are needed to optimize the transport properties of a material.

Nevertheless, the results above show that employing a CRT with $\tau_0 = 10^{-13} \text{ s}$ can give a reasonably good description of Mg₂Si as long as the charge carrier concentration is chosen according to what is available experimentally. This gives confidence that this setting can be used for the high-throughput screening. The optimistic selections of parameters may be realistic in some cases (particularly for low optimal charge carrier concentrations) but can be expected to yield too favorable transport properties in other cases, even when sufficiently high doping levels are available.

B. High-throughput screening

The predicted optimal figure of merit ZT_0 is plotted as a function of the optimal (n- or p-doped) carrier concentration for all materials with $ZT_0 > 0.1$ in Fig. 5. Most materials have $ZT_0 < 0.1$ and are thus not visible in the plots. Each bubble in this plot represents a material system like Mg₂Si, with the bubble size

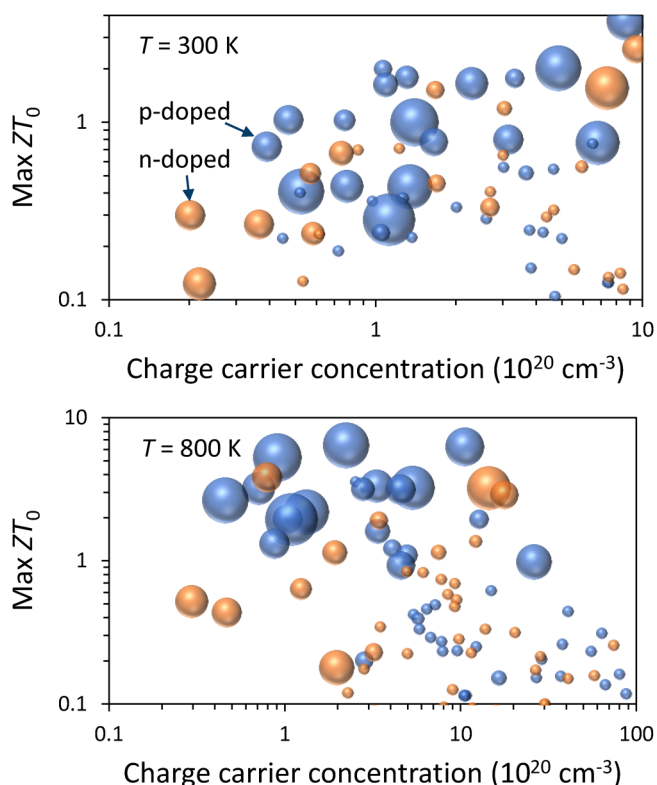


FIG. 5. Bubble plot of the predicted figure of merit as a function of charge carrier concentration of the most promising compounds at $T = 300 \text{ K}$ (upper chart) and 800 K (lower chart). p- and n-doped compounds are shown as blue and orange bubbles. The bubble size designates the DFT-calculated bandgap, ranging between 0.05 and 1.08 eV. Compounds with bandgaps below 0.05 eV or 0 are shown with a size corresponding to 0.05 eV.

designating the DFT-predicted bandgap of the material. (Small or zero bandgap materials are shown as small bubbles.) At 300 K, there is a clear correspondence between the highest ZT_0 values and the required charge carrier concentrations; around $5 \times 10^{19} \text{ cm}^{-3}$ is, e.g., needed to obtain $ZT_0 = 1$, and the highest ZT_0 values are found around 10^{21} cm^{-3} . This emphasizes the need for highly doped systems in thermoelectricity in order to optimize the figure of merit. Turning to $T = 800 \text{ K}$, the correlation between ZT_0 and the carrier concentration is less clear. This is partially due to increasing contributions from minority charge carriers, particularly for low bandgap materials. This results in optimal charge concentrations that are even higher than those for 300 K, but with corresponding ZT_0 values that are actually lower for the highest carrier concentrations. Almost all the best materials have relatively large bandgaps at $T = 800 \text{ K}$, which is beneficial at a high temperature to avoid bipolar conduction.

The most promising compounds identified by the high-throughput screening are summarized in Table I. ZT_0 values have been listed for $T = 300$ and 800 K , representing room-temperature and high-temperature applications. Only compounds with $ZT_0 > 1$

TABLE I. The most promising silicides for thermoelectric applications predicted from the high-throughput transport calculations using CRT with $\tau_0 = 10^{-13}$ s. p-doped (n-doped) materials are listed in the upper (lower) part of the table. The calculations have been performed at room temperature (300 K) and at $T = 800$ K. The predicted maximal figure of merit ZT_0 has been listed along with the correspondingly required (optimal) charge carrier concentration (p_c for p-doped and n_c for n-doped). Only those compounds with $ZT_0 > 1.0$ at $T = 300$ or 800 K have been listed and will be used for the high-accuracy calculations.

p-doped			T = 300 K		T = 800 K	
Composition	Space group	Bandgap (eV)	Max ZT_0	Required p_c (10^{20} cm^{-3})	Max ZT_0	Required p_c (10^{20} cm^{-3})
Ca ₂ Si	<i>Fm$\bar{3}m$</i>	0.59	3.72	8.67	6.29	10.55
Ba ₃ (SiAs ₂) ₂	<i>C2/c</i>	0.83	2.02	4.84	6.43	2.23
Li ₂ MgSi	<i>F43m</i>	0.13	2.00	1.06	1.22	4.08
Cu ₂ SiSe ₃	<i>Cc</i>	0.22	1.80	1.31	3.17	2.78
FeSiW	<i>F43m</i>	0.15	1.77	3.32	1.95	12.69
SrCaSi	<i>Pnma</i>	0.43	1.66	2.29	3.34	3.32
Mg ₂ Si	<i>Fm$\bar{3}m$</i>	0.24	1.63	1.09	1.61	3.36
AlSiP ₃	<i>Pnma</i>	0.35	1.03	0.47	1.96	1.03
BaCaSi	<i>Pnma</i>	0.18	1.03	0.76	1.10	4.94
Sr ₃ (SiAs ₂) ₂	<i>C2/c</i>	0.92	1.00	1.40	5.29	0.90
Cu ₈ SiSe ₆	<i>Pmn2₁</i>	0.36	0.80	3.14	3.16	4.54
Mn ₄ Si ₇	<i>P4c2</i>	0.76	0.77	6.79	3.25	5.32
SiGe	<i>P6₃mc</i>	0.36	0.73	0.39	1.32	0.87
FeSi ₂	<i>Cmce</i>	0.00	0.56	3.01	3.57	2.52
Ba ₃ (Si ₂ P ₃) ₂	<i>P2₁/m</i>	0.43	0.44	0.78	3.22	0.71
BaSi ₂	<i>Pnma</i>	0.80	0.43	1.34	2.20	1.32
Ca ₃ (SiAs ₂) ₂	<i>P2₁/c</i>	0.83	0.41	0.52	2.65	0.46
SiAs ₂	<i>Pbam</i>	1.08	0.28	1.12	1.95	1.09
n-doped			T = 300 K		T = 800 K	
Composition	Space group	Bandgap (eV)	Max ZT_0	Required n_c (10^{20} cm^{-3})	Max ZT_0	Required n_c (10^{20} cm^{-3})
TiFe ₂ Si	<i>Fm$\bar{3}m$</i>	0.32	2.59	9.49	2.89	17.67
Mn ₄ Si ₇	<i>Pcca</i>	0.75	1.56	7.36	3.23	14.45
Na(LiSi ₂) ₃	<i>Pnma</i>	0.13	1.52	1.67	1.91	3.42
Ba ₂ LiSi ₃	<i>Fddd</i>	0.09	1.20	3.04	1.15	7.47
Mg ₂ Si	<i>Fm$\bar{3}m$</i>	0.24	0.67	0.74	1.14	1.92
WSi ₂	<i>P6₂22</i>	0.07	0.56	5.92	1.37	12.15
SiGe	<i>P6₃mc</i>	0.36	0.30	0.20	3.84	0.79

at either temperature have been included in the list, resulting in 18 p-doped and 7 n-doped systems. Three materials are listed as promising for both p- and n-doping: Mn₄Si₇, Mg₂Si, and SiGe. Also shown is the charge carrier concentration corresponding to the optimal chemical potential, as demonstrated for Mg₂Si in Fig. 2.

It is reassuring that the already well-established silicides with good TE properties, such as Mg₂Si, Mn₄Si₇, and SiGe, are found among the most promising compounds. This strengthens the assumption that important candidate materials are not overlooked with the screening procedure. Nonetheless, to get more robust predictions of the materials in Table I, more accurate calculations were performed for those materials, presented in Sec. III C.

C. High-accuracy calculations

The results in Table II have been produced by using the deformation potential to predict electron relaxation times within the acoustic phonon scattering mechanism. Temperature-dependent

phonon thermal conductivity has been provided for four of the systems; for the remaining systems, the values from Mg₂Si were used.

We note that the longitudinal sound velocity v_l displays values between 4.0 and 11.5 km/s, while the deformation potential constant E_1 varies between 3.4 and 12.1 eV. Since the acoustic phonon electron relaxation time τ^{AP} varies as v_l^2/E_1^2 , this has a strong influence on the relaxation time and thus the various transport properties.

The phonon thermal conductivity κ_{ph} was calculated assuming 25% Sn substituted on the Si sites and grain boundary scattering with a typical grain size of 50 nm. This led to very low values of κ_{ph} (around or below $1 \text{ W m}^{-1} \text{ K}^{-1}$) in the case of Mg₂Si, Li₂MgSi, and Ca₂Si. However, FeSiW displays values of κ_{ph} between 3 and $4 \text{ W m}^{-1} \text{ K}^{-1}$ leading to a significant reduction of the optimal figure of merit. It can be expected that this is the case also for other materials in Table II. We have nevertheless used the κ_{ph} values from Mg₂Si for the other systems to give an upper estimate of ZT_0 from the present results.

This still leads to a significant reduction of ZT_0 for many of the systems. Only eight p-doped and two n-doped systems remain

TABLE II. The most promising silicides for thermoelectric applications predicted from high-accuracy transport calculations using acoustic phonon scattering to predict the electron relaxation times. The longitudinal sound velocity v_l and deformation potential E_1 needed to calculate the electron relaxation time are listed. In addition, the phonon thermal conductivity κ_{ph} , optimal figure of merit ZT_0 , and the required charge carrier concentration are shown for temperatures $T = 300$ and 800 K. p-doped (n-doped) materials are listed in the upper (lower) part of the table. Some numbers are missing due to problems with convergence or too high computational cost. In those cases, the corresponding values of Mg_2Si were used to calculate the figure of merit.

Composition	p-doped					$T = 300$ K					$T = 800$ K				
	Sound velocity v_l (km/s)	Deform. potential E_1 (eV)	Thermal cond. κ_{ph} (W/mK)	Max ZT_0	Required n (10^{20} cm^{-3})	Thermal cond. κ_{ph} (W/mK)	Max ZT_0	Required n (10^{20} cm^{-3})	Thermal cond. κ_{ph} (W/mK)	Max ZT_0	Required n (10^{20} cm^{-3})	Thermal cond. κ_{ph} (W/mK)	Max ZT_0	Required n (10^{20} cm^{-3})	
Mg_2Si	6.6	12.1	1.09	2.33	2.50	0.83	1.72	10.08	0.83	1.72	10.08	0.83	1.72	10.08	
Li_2MgSi	6.9	10.5	0.65	1.72	7.26	0.44	1.17	17.00	0.44	1.17	17.00	0.44	1.17	17.00	
$Ca_3(SiAs_2)_2$	5.3	4.8	...	1.29	0.30	...	2.22	0.33	...	2.22	0.33	...	2.22	0.33	
$AlSiP_3$	11.5	13.1	...	1.26	0.31	...	2.34	0.61	...	2.34	0.61	...	2.34	0.61	
$SiGe$	6.7	1.06	0.28	...	1.45	0.48	...	1.45	0.48	...	1.45	0.48	
$FeSi_2$	10.1	5.2	...	0.95	0.66	...	1.64	1.57	...	1.64	1.57	...	1.64	1.57	
$SiAs_2$	5.4	3.4	...	0.54	4.26	...	1.36	1.04	...	1.36	1.04	...	1.36	1.04	
Mn_4Si_7	9.7	5.7	...	0.52	3.94	...	1.22	6.64	...	1.22	6.64	...	1.22	6.64	
$Sr_3(SiAs_2)_2$	4.5	6.0	...	0.42	0.97	...	0.73	1.51	...	0.73	1.51	...	0.73	1.51	
$Ba_3(Si_2P_3)_2$	6.5	10.2	...	0.39	1.27	...	0.99	1.50	...	0.99	1.50	...	0.99	1.50	
$Ba_3(SiAs_2)_2$	4.0	6.3	...	0.32	3.03	...	0.50	4.60	...	0.50	4.60	...	0.50	4.60	
$BaCaSi$	4.3	6.9	...	0.27	0.70	...	0.10	6.04	...	0.10	6.04	...	0.10	6.04	
$SrCaSi$	5.1	8.9	...	0.26	1.84	...	0.40	4.63	...	0.40	4.63	...	0.40	4.63	
$FeSiW$	6.2	8.7	3.92	0.22	1.18	3.07	0.24	8.96	3.07	0.24	8.96	3.07	0.24	8.96	
Cu_2SiSe_3	5.3	0.18	1.60	...	0.41	11.47	...	0.41	11.47	...	0.41	11.47	
Ca_2Si	5.4	10.4	0.82	0.13	20.58	0.56	0.49	89.49	0.56	0.49	89.49	0.56	0.49	89.49	
$BaSi_2$	5.4	11.4	...	0.06	0.55	...	0.11	1.41	...	0.11	1.41	...	0.11	1.41	
Cu_8SiSe_6	4.0	0.04	1.95	...	0.13	11.78	...	0.13	11.78	...	0.13	11.78	
Composition	n-doped					$T = 300$ K					$T = 800$ K				
	Sound velocity v_l (km/s)	Deform. potential E_1 (eV)	Thermal cond. κ_{ph} (W/mK)	Max ZT_0	Required n (10^{20} cm^{-3})	Thermal cond. κ_{ph} (W/mK)	Max ZT_0	Required n (10^{20} cm^{-3})	Thermal cond. κ_{ph} (W/mK)	Max ZT_0	Required n (10^{20} cm^{-3})	Thermal cond. κ_{ph} (W/mK)	Max ZT_0	Required n (10^{20} cm^{-3})	
Mg_2Si	6.6	12.1	1.09	3.55	5.54	0.83	2.31	4.55	0.83	2.31	4.55	0.83	2.31	4.55	
$Na(LiSi_2)_3$	9.1	3.2	...	2.23	0.30	...	1.87	0.99	...	1.87	0.99	...	1.87	0.99	
$TiFe_2Si$	7.5	5.1	...	0.93	8.38	...	0.16	22.40	...	0.16	22.40	...	0.16	22.40	
$SiGe$	6.7	0.32	0.47	...	0.41	1.65	...	0.41	1.65	...	0.41	1.65	
Ba_2LiSi_3	5.1	11.9	...	0.24	3.54	...	0.28	6.81	...	0.28	6.81	...	0.28	6.81	
WSi_2	5.0	8.0	...	0.15	9.73	...	0.36	13.75	...	0.36	13.75	...	0.36	13.75	
Mn_4Si_7	...	5.8	...	0.00	1.70	...	0.17	3.12	...	0.17	3.12	...	0.17	3.12	

with $ZT_0 > 1$ in Table II. Some of them require very high doping levels to attain the highest figure of merit (e.g., $\sim 10^{21} \text{ cm}^{-3}$ for Mg_2Si and Li_2MgSi), which means that the realistic values are probably lower. This is illustrated for Mg_2Si in Fig. 4, where lower charge carrier concentrations were used to obtain reasonable correspondence with experiments. Tedious defect chemistry calculations would be required to predict the solubility of dopants and abundance of intrinsic defects, thus giving realistic doping levels from first-principles calculations.

As illustrated in Fig. 4, acoustic phonon scattering is not necessarily describing the electron scattering of all the systems properly. Even if the relaxation times are predicted without fitting of empirical parameters, other scattering mechanisms may be dominating at some or all the temperatures of this study. This means that the materials with significantly lower ZT_0 values in Table II than in Table I should not be disregarded completely; if neutral defect scattering is the dominant mechanism, the values in Table I may still be realistic within the limitations discussed above. Materials from both tables will thus be included in the forthcoming discussion.

D. Discussion

As anticipated in the discussion on Mg_2Si above, the quantitative correspondence between the calculated ZT_0 and the maximal experimental ZT for the known materials is not always very good. For example, in the case of higher manganese silicides (HMS), represented by Mn_4Si_7 , the maximum experimental p-type ZT is 0.15 and 0.6 at $T = 300$ and 800 K ,⁵⁷ while the corresponding predicted values are 0.8 and 3.3 (CRT scattering, Table I) or 0.5 and 1.2 (AP scattering, Table II). Like in the case for p-doped Mg_2Si , this discrepancy can be understood from the high optimal charge carrier concentration (ranging up to $\sim 10^{21} \text{ cm}^{-3}$ both experimentally and theoretically), which most likely is not experimentally accessible. Also, it is probably not compatible with the optimistic, fixed CRT. The high intrinsic p-doping levels of HMS make it difficult to obtain high n-doping of this system, which means that the very high CRT-predicted ZT_0 values for n-doped Mn_4Si_7 are not likely to be obtained experimentally.

For the Si-Ge system, the highest experimental ZT is typically ~ 0.5 at 300 K and ~ 1.3 at 800 K , for both n-doped⁵⁸ (with an optimal charge carrier concentration of $n_c \sim 10^{20} \text{ cm}^{-3}$) and p-doped⁵⁹ ($p_c \sim 5 \times 10^{20} \text{ cm}^{-3}$) materials. This cannot be directly compared to the predicted numbers above; while the unit cell used for the modeling is periodic with stoichiometry SiGe , the real materials exhibit solid solubility and an optimal composition of $\text{Si}_{80}\text{Ge}_{20}$.^{58,59} The good correspondence between experiment and the p-doped ZT_0 values of Tables I and II is thus most likely due to a fortuitous cancellation of errors.

The list in Table I also contains materials where TE properties are known from experiments, but where the experimental ZT is significantly lower than predicted in the present work: Ca_2Si , FeSi_2 , BaSi_2 , and WSi_2 . The most promising of those in Table I is p-doped Ca_2Si . While the stable version of Ca_2Si in ambient conditions is orthorhombic,⁶⁰ this is the cubic version of Ca_2Si with a similar crystal structure as Mg_2Si . The cubic allotrope can be obtained by straining the system and has been investigated in a few

TE studies in the literature.^{60–62} A recent modeling study reported ZT_0 values around one order of magnitude lower than the present paper.⁶² This can be explained by their choice of a smaller electron relaxation time ($\tau = 10^{-15} \text{ s}$) and that their thermal conductivity was higher, based on phonon predictions without alloying. If we turn to the AP scattering results in Table II, however, the ZT_0 values are significantly lower and require extremely high carrier concentrations. Overall, this makes it unlikely that Ca_2Si is feasible for TE applications. Experimental results on TE properties are only available for the orthorhombic allotrope.⁶³

In the case of FeSi_2 , none of the experimental studies listed in Ref. 9 have achieved sufficiently high charge carrier concentration to obtain anything near the promising p-type performance in both Tables I and II, requiring $p_c \sim 0.5\text{--}2.5 \times 10^{20} \text{ cm}^{-3}$. Two studies have investigated the TE properties of BaSi_2 ,^{64,65} but they only tried n-doped, possibly overlooking the potential of p-doped BaSi_2 inferred from CRT—but the AP results are not very favorable, casting a doubt on the promise of this material. The hexagonal form of WSi_2 ⁶⁶ is metastable,^{67,68} and only one study has reported TE properties that have not been optimized of this material.⁶⁹ This material also shows significantly reduced ZT_0 values when going from CRT to AP scattering.

When turning to the novel materials listed in Table I, we should keep in mind that the predicted ZT_0 values are likely to exaggerate the TE potential of many of the materials. Indeed, many of the CRT-calculated values are significantly higher than any reproducible experimental ZT values of any material in the literature. The highest confirmed experimental ZT values are around 2–2.5,⁷⁰ while many of the listed ZT_0 values are higher than 3, particularly at 800 K . This is caused by the universal, optimistic values of the CRT and thermal conductivity that were selected to fit those known for Mg_2Si , combined with the possibility to dope any material to arbitrary levels.

One of the promising novel materials is the Heusler compound TiFe_2Si , displaying the highest performance among the n-doped materials. This compound is included in the Materials Project database as potentially stable,³⁶ but its existence has so far not been confirmed experimentally. There is a quite large difference between the CRT- and AP-predicted ZT_0 values. Also, the CRT-required charge carrier concentration is very high, in the order of 10^{21} cm^{-3} ; TiFe_2Si thus has a quite high risk to be unfeasible for TE applications.

Li_2MgSi has a cubic crystal structure and has been studied somewhat in the literature as a potential Li anode material.^{71,72} The optimal p_c is $\sim 10^{20} \text{ cm}^{-3}$ and the corresponding ZT_0 is similar to that of Mg_2Si when using CRT scattering. Similar ZT_0 values are obtained with AP scattering, albeit at higher carrier concentrations. This is a very interesting material to investigate further for TE purposes.

Many of the promising materials listed in Table I are Zintl compounds—intermetallic compounds where low electronegativity elements (typically alkali or earth-alkaline metals) connect to high electronegativity elements (e.g., post-transition metals or metalloids, including Si), displaying both ionic and covalent bonds.⁷³ Zintl compounds usually display small bandgaps that are beneficial for TE applications, but they are often brittle, which may be an obstacle for technological usage. Most of these candidates have

barely had their crystal structure identified, with no TE properties determined: $\text{Ba}_3(\text{SiAs}_2)_2$,⁷⁴ SrCaSi ,⁷⁵ BaCaSi (investigated as a topological material),⁷⁶ $\text{Sr}_3(\text{SiAs}_2)_2$,⁷⁷ $\text{Ba}_3(\text{Si}_2\text{P}_3)_2$,⁷⁸ $\text{Ca}_3(\text{SiAs}_2)_2$,⁷⁷ and Ba_2LiSi_3 .⁷⁹ Some of these materials exhibit strongly reduced ZT_0 values when moving from CRT to AP scattering, but others remain promising from a theoretical point of view. It is unclear whether any of them are feasible for technological application or even testing of functional properties.

Likewise, many of the other compounds in Table I have only been reported in the literature once or a few times, with focus on the crystal structure determination and no reported TE properties: the monoclinic Cu_2SiSe_3 ,⁸⁰ the Laves phase FeSiW ,⁸¹ the AlSiP_3 compound displaying a wurtzite-pyrite intergrowth structure,⁸² the tetrahedrally close-packed Cu_8SiSe_6 ,⁸³ the layered SiAs_2 ,^{84,85} (transport properties were not possible to measure because of unsuccessful attempts to produce a compact pellet⁸⁵), and the orthorhombic $\text{Na}(\text{LiSi}_2)_3$.⁸⁶ All of these lack experimental information to judge their potential as TE materials, which suggests that they may be interesting for future experimental studies. Information from both Tables I and II should be used to guide such efforts.

As mentioned above, the parameters for the transport calculations have been selected to minimize the number of false negatives, i.e., reducing the risk of overlooking potentially promising systems. This does not mean that this risk is negligible. Most importantly, using the GGA means that bandgaps are systematically underestimated in the present study. Several materials with a small bandgap can thus have been predicted to be metallic, which reduces the chance of predicting TE properties correctly significantly. Also, too small bandgaps may overestimate the contribution from minority carriers, particularly at a higher temperature. Furthermore, the band shape predicted by GGA is not always accurate, and we cannot disregard that systems with a high degree of band convergence have been ignored by the present study.

Nevertheless, we can expect that the largest errors of this screening study can be found in the opposite direction: false positives, i.e., promising predictions that are not correct. The first and most obvious source of this is as mentioned before, the constant, optimistic values of τ_0 and κ_{ph} . In addition, several other assumptions have been made that may be only partially fulfilled experimentally.

One important assumption is dopability, i.e., that the optimal doping concentration (and thus charge carrier concentration as seen in Fig. 2) can be reached experimentally. This is not necessarily true for many materials, in which case the transport properties would reach sub-optimal values in an experimental study.

Another presumption is that a low κ_{ph} can be reached by alloying. This was implicit in the high-throughput part but was explicitly used to calculate κ_{ph} from first-principles calculations in the high-accuracy part. Isoelectronic substitution on one site (alloying) can typically reduce κ_{ph} to a fraction, particularly when the pure material has a high κ_{ph} .^{29,50} But this can only be achieved if the substitute is soluble in the pure material; otherwise, phase separation will instead take place. (Phase separation can in some cases be positive for TE properties,⁸⁷ but relying on this would be another assumption that has to be taken.)

Many of the materials listed in Table I have only been reported in studies where the crystal structure has been determined

with powder x-ray diffraction. It is thus difficult to know whether they are feasible to synthesize in a form with mechanical integrity adequate for measurement of TE properties or application as functional materials. Also, some of these materials may have a low melting point, decomposition temperature, or a (unreported) phase transformation that would hinder technological exploitation. This can currently only be tested experimentally.

Some of the listed materials have relatively high bandgaps, reaching up to (and even slightly beyond) 1 eV. Since these are likely to be underestimated, some of the promising materials may turn out to have such a high bandgap that their predicted TE properties are not available experimentally. In practice, this would manifest itself as a resistance to reaching the optimal charge carrier concentration.

Despite the various pitfalls, the ability to point out the silicides with highest TE figure of merit among around 1000 candidates supports the belief that other, presently unknown materials with good TE properties can be found among the 18 new materials systems with $ZT_0 > 1$ listed in Table I. They may have a lower figure of merit than what is listed in the table but could still be interesting from a cost-benefit perspective, since many of the promising candidates are based on non-toxic, abundant elements. Even if a material turns out to be difficult to optimize completely and the optimal carrier concentration cannot be obtained experimentally, the resulting TE properties can still be good enough for applications.

An extension of the present study would be to rule out more of the candidate systems with more elaborate and expensive calculations. This could be done on a selection of systems with quite good predicted properties, e.g., $ZT_0 > 0.1$ (this includes 72 systems of the present study). It would be feasible to conduct an elaborate study on such a small subset, combining the high-accuracy methods described above (determining the temperature-dependent electron relaxation time from electron-phonon scattering calculations,¹³ a realistic temperature-dependent phonon thermal conductivity from phonon calculations including grain boundary and alloy scattering²⁹) with a test of the alloying possibility¹¹ and dopability.⁸⁸ This would have given an even more focused recommendation of systems to study experimentally than the present work and should be the topic of a future investigation.

IV. CONCLUSIONS

Transport calculations based on density functional theory and the Boltzmann transport equation were used to predict the TE figure of merit for all known crystalline silicides except rare, expensive, toxic, and radioactive ones. Oxides, hydrides, carbides, and halides were also neglected. The screening was summarized in a list of promising compounds with a predicted figure of merit $ZT_0 > 1$ (Table I). This consisted of 18 p-doped and 7 n-doped materials, of which 3 compounds were present in both lists. The TE properties of 7 of these 22 compounds have been investigated experimentally in the literature, but not all of them extensively. The remaining 15 of the promising compounds are only scarcely investigated in the literature, and no experimental studies of their TE properties are available.

The electronic relaxation time and phonon thermal conductivity were used as adjustable parameters and optimistic values were

selected to avoid overlooking promising systems in the high-throughput screening. This means that the predicted figure of merit is likely to be higher than experimentally feasible for many of the materials. Nevertheless, the methodology predicted successfully the thermoelectric potential of the best silicide materials known from experiments: Mg_2Si , MnSi_x , and SiGe . This lends support to the assumption that most promising materials will be discovered by the technique.

The promising compounds were studied in a final, high-accuracy step where the temperature-dependent phonon thermal conductivity was calculated for some of the compounds and the electron relaxation time was calculated for all of them using acoustic phonon scattering based on the deformation potential method. This led to a reduced predicted ZT_0 of many of the materials. Eight p-doped and two n-doped systems remain with $ZT_0 > 1$ at this theoretical level. Since the electron scattering mechanism may change between materials, both predictions should be taken into account when deciding whether to investigate a system further.

For all the new promising compositions, it remains to be proven that they may be doped to sufficiently high levels, that appropriate alloying can be used to reduce phonon thermal conductivity sufficiently, and that they are thermodynamically stable at relevant temperatures. We recommend investigating this experimentally and theoretically.

ACKNOWLEDGMENTS

Financial support from the Research Council of Norway through the TESil project (Grant No. 269326) is gratefully acknowledged, and the authors appreciate fruitful discussions with the project team. The computations were performed with a grant from the Norwegian e-infrastructure for Research and Education, Sigma2.

DATA AVAILABILITY

The data that support the findings of this study are available from the corresponding author upon reasonable request.

REFERENCES

- W. He, G. Zhang, X. X. Zhang, J. Ji, G. Q. Li, and X. D. Zhao, *Appl. Energy* **143**, 1 (2015).
- G. D. Mahan, *APL Mater.* **4**, 104806 (2016).
- M. Dresselhaus, *AIP Conf. Proc.* **1519**, 36 (2013).
- E. Flage-Larsen and O. M. Løvvik, "Band structure guidelines for higher figure-of-merit: Analytic band generation and energy filtering," in *Thermoelectrics and Its Energy Harvesting*, edited by D. M. Rowe (CRC Press Inc., 2012).
- O. M. Løvvik and K. Berland, *Mater. Today Proc.* **5**, 10227 (2018).
- K. Berland, X. Song, P. A. Carvalho, C. Persson, T. G. Finstad, and O. M. Løvvik, *J. Appl. Phys.* **119**, 125103 (2016).
- G. J. Snyder and E. S. Toberer, *Nat. Mater.* **7**, 105 (2008).
- A. Zevalkink, D. M. Smiadak, J. L. Blackburn, A. J. Ferguson, M. L. Chabinyk, O. Delaire, J. Wang, K. Kovnir, J. Martin, L. T. Schelhas, T. D. Sparks, S. D. Kang, M. T. Dylla, G. J. Snyder, B. R. Ortiz, and E. S. Toberer, *Appl. Phys. Rev.* **5**, 021303 (2018).
- A. Nozariasmarz, A. Agarwal, Z. A. Coutant, M. J. Hall, J. Liu, R. Liu, A. Malhotra, P. Norouzzadeh, M. C. Öztürk, V. P. Ramesh, Y. Sargolzaeiaval, F. Suarez, and D. Vashaee, *Jpn. J. Appl. Phys.* **56**, 05DA04 (2017).
- J. de Boor, S. Gupta, H. Kolb, T. Dasgupta, and E. Müller, *J. Mater. Chem. C* **3**, 10467 (2015).
- S. Bhattacharya and G. K. H. Madsen, *Phys. Rev. B* **92**, 085205 (2015).
- V. G. Tyuterev, S. V. Obukhov, N. Vast, and J. Sjakste, *Phys. Rev. B* **84**, 035201 (2011).
- Z. Wang, S. D. Wang, S. Obukhov, N. Vast, J. Sjakste, V. Tyuterev, and N. Mingo, *Phys. Rev. B* **83**, 205208 (2011).
- M. Schrade, K. Berland, S. N. H. Eliassen, M. N. Guzik, C. Echevarria-Bonet, M. H. Sørby, P. Jenus, B. C. Hauback, R. Tofan, A. E. Gunnæs, C. Persson, O. M. Løvvik, and T. G. Finstad, *Sci. Rep.* **7**, 1–10 (2017).
- K. Berland and C. Persson, *Comput. Mater. Sci.* **134**, 17 (2017).
- K. Berland and C. Persson, *J. Appl. Phys.* **123**, 205703 (2018).
- See <https://github.com/espenfl/t4me> for "Transport 4 Materials, T4ME" (accessed 30 December 2019).
- N. Tandon, J. D. Albrecht, and L. R. Ram-Mohan, *Diamond Relat. Mater.* **56**, 1 (2015).
- Q. Xu, J. W. Zhou, T. H. Liu, and G. Chen, *Appl. Phys. Lett.* **115**, 023903 (2019).
- O. Hellman and D. A. Broido, *Phys. Rev. B* **90**, 134309 (2014).
- N. Shulumba, O. Hellman, and A. J. Minnich, *Phys. Rev. B* **95**, 014302 (2017).
- J. D. Querales-Flores, J. Cao, S. Fahy, and I. Savić, *Phys. Rev. Mater.* **3**, 055405 (2019).
- W. Chen, J.-H. Pöhls, G. Hautier, D. Broberg, S. Bajaj, U. Aydemir, Z. M. Gibbs, H. Zhu, M. Asta, G. J. Snyder, B. Meredig, M. A. White, K. Persson, and A. Jain, *J. Mater. Chem. C* **4**, 4414 (2016).
- M. W. Gaultois, T. D. Sparks, C. K. H. Borg, R. Seshadri, W. D. Bonificio, and D. R. Clarke, *Chem. Mater.* **25**, 2911 (2013).
- J. Carrete, N. Mingo, S. D. Wang, and S. Curtarolo, *Adv. Funct. Mater.* **24**, 7427 (2014).
- G. K. H. Madsen, *J. Am. Chem. Soc.* **128**, 12140 (2006).
- M. Miyata, T. Ozaki, T. Takeuchi, S. Nishino, M. Inukai, and M. Koyano, *J. Electron. Mater.* **47**, 3254 (2018).
- A. Jain, Y. Shin, and K. A. Persson, *Nat. Rev. Mater.* **1**, 15004 (2016).
- K. Berland, N. Shulumba, O. Hellman, C. Persson, and O. M. Løvvik, *J. Appl. Phys.* **126**, 145102 (2019).
- X. Li, L. L. Xi, and J. Yang, *J. Inorg. Mater.* **34**, 236 (2019).
- G. K. H. Madsen and D. J. Singh, *Comput. Phys. Commun.* **175**, 67 (2006).
- W. Chen, J. H. Pöhls, G. Hautier, D. Broberg, S. Bajaj, U. Aydemir, Z. M. Gibbs, H. Zhu, M. Asta, G. J. Snyder, B. Meredig, M. A. White, K. Persson, and A. Jain, *J. Mater. Chem. C* **4**, 4414 (2016).
- G. Kresse and J. Furthmüller, *Phys. Rev. B* **54**, 11169 (1996).
- G. Kresse and J. Hafner, *Phys. Rev. B* **47**, 558 (1993).
- J. Merkisz, P. Fuc, P. Lijewski, K. Wojciechowski, and R. Zybala, "Test bed study of waste heat recovery from the exhaust of a spark ignition engine," in *Proceedings of the Ninth Asia-Pacific International Symposium on Combustion and Energy Utilization*, edited by X. Q. Zhang and X. Liu (World Publishing Corporation, 2008), p. 439.
- A. Jain, K. A. Persson, and G. Ceder, *APL Mater.* **4**, 053102 (2016).
- See https://en.wikipedia.org/wiki/Restriction_of_Hazardous_Substances_Directive for "Restriction of Hazardous Substances Directive" (accessed 30 December 2019).
- "Abundance of elements in the earth's crust and in the sea," in *CRC Handbook of Chemistry and Physics*, 97th ed., edited by W. M. Haynes (CRC Press, 2016–2017), p. 14.
- See https://en.wikipedia.org/wiki/Prices_of_elements_and_their_compounds for "Prices of elements and their compounds" (accessed 30 December 2019).
- J. P. Perdew, K. Burke, and M. Ernzerhof, *Phys. Rev. Lett.* **77**, 3865 (1996).
- G. Kresse and D. Joubert, *Phys. Rev. B* **59**, 1758 (1999).
- N. W. Ashcroft and N. D. Mermin, *Solid State Physics* (Harcourt College Publishers, 1976).
- J. Bardeen and W. Shockley, *Phys. Rev.* **80**, 72 (1950).
- C. Jacoboni, *Theory of Electron Transport in Semiconductors: A Pathway From Elementary Physics to Nonequilibrium Green Functions* (Springer, Berlin, 2010).
- S.-H. Wei and A. Zunger, *Phys. Rev. B* **60**, 5404 (1999).
- Y. Le Page and P. Saxe, *Phys. Rev. B* **65**, 104104 (2002).

- ⁴⁷O. Hellman, I. A. Abrikosov, and S. I. Simak, *Phys. Rev. B* **84**, 180301 (2011).
- ⁴⁸H.-S. Kim, Z. M. Gibbs, Y. Tang, H. Wang, and G. J. Snyder, *APL Mater.* **3**, 041506 (2015).
- ⁴⁹E. Flage-Larsen and O. Prytz, *Appl. Phys. Lett.* **99**, 202108 (2011).
- ⁵⁰S. N. H. Eliassen, A. Katre, G. K. H. Madsen, C. Persson, O. M. Løvvik, and K. Berland, *Phys. Rev. B* **95**, 045202 (2017).
- ⁵¹N. Satyala, J. S. Krasinski, and D. Vashaee, *Acta Mater.* **74**, 141 (2014).
- ⁵²K. Arai, A. Sasaki, Y. Kimori, M. Iida, T. Nakamura, Y. Yamaguchi, K. Fujimoto, R. Tamura, T. Iida, and K. Nishio, *Mater. Sci. Eng. B* **195**, 45 (2015).
- ⁵³W. Liu, X. J. Tan, K. Yin, H. J. Liu, X. F. Tang, J. Shi, Q. J. Zhang, and C. Uher, *Phys. Rev. Lett.* **108**, 166601 (2012).
- ⁵⁴X. H. Liu, L. L. Xi, W. J. Qiu, J. Yang, T. J. Zhu, X. B. Zhao, and W. Zhang, *Adv. Electron. Mater.* **2**, 1500284 (2016).
- ⁵⁵J. de Boer, T. Dasgupta, U. Saparamadu, E. Müller, and Z. F. Ren, *Mater. Today Energy* **4**, 105 (2017).
- ⁵⁶P. Gao, J. D. Davis, V. V. Poltavets, and T. P. Hogan, *J. Mater. Chem. C* **4**, 929 (2016).
- ⁵⁷V. Ponnambalam, D. T. Morelli, S. Bhattacharya, and T. M. Tritt, *J. Alloys Compd.* **580**, 598 (2013).
- ⁵⁸X. W. Wang, H. Lee, Y. C. Lan, G. H. Zhu, G. Joshi, D. Z. Wang, J. Yang, A. J. Muto, M. Y. Tang, J. Klatsky, S. Song, M. S. Dresselhaus, G. Chen, and Z. F. Ren, *Appl. Phys. Lett.* **93**, 193121 (2008).
- ⁵⁹S. Ahmad, A. Singh, A. Bohra, R. Basu, S. Bhattacharya, R. Bhatt, K. N. Meshram, M. Roy, S. K. Sarkar, Y. Hayakawa, A. K. Debnath, D. K. Aswal, and S. K. Gupta, *Nano Energy* **27**, 282 (2016).
- ⁶⁰C. L. Wen, Q. H. Xie, R. Xiong, B. S. Sa, N. H. Miao, J. Zhou, B. Wu, and Z. M. Sun, *Europhys. Lett.* **123**, 67003 (2018).
- ⁶¹M. Rittirum, S. Hemathulin, S. Yokhasing, K. Matarat, and T. Seetawan, *Mater. Today Proc.* **5**, 14052 (2018).
- ⁶²R. Xiong, B. S. Sa, N. H. Miao, Y. L. Li, J. Zhou, Y. C. Pan, C. L. Wen, B. Wu, and Z. M. Sun, *RSC Adv.* **7**, 8936 (2017).
- ⁶³C. Wen, T. Nonomura, A. Kato, Y. Kenichi, H. Udono, K. Isobe, M. Otake, Y. Kubota, T. Nakamura, Y. Hayakawa, and H. Tatsuoka, "Electrical properties of Ca₂Si sintered compact synthesized by spark plasma sintering," in *Asia-Pacific Conference on Semiconducting Silicides Science and Technology Towards Sustainable Optoelectronics*, edited by Y. Maeda (Elsevier Science BV, 2011), Vol. 11, p. 106.
- ⁶⁴K. Hashimoto, K. Kurosaki, H. Muta, and S. Yamanaka, *Mater. Trans.* **49**, 1737 (2008).
- ⁶⁵Y. D. Xu, Y. X. Wu, Z. W. Chen, W. J. Shen, Z. Z. Jian, S. Q. Lin, J. Li, W. Li, and Y. Z. Pei, *Funct. Mater. Lett.* **9**, 1650017 (2016).
- ⁶⁶F. M. d'Heurle, C. S. Petersson, and M. Y. Tsai, *J. Appl. Phys.* **51**, 5976 (1980).
- ⁶⁷Y. Pan, C. Jing, and Y. P. Wu, *Vacuum* **167**, 374 (2019).
- ⁶⁸C. Krontiras, I. Suni, F. M. d'Heurle, F. K. LeGoues, and R. Joshi, *J. Phys. F Metal Phys.* **17**, 1953 (1987).
- ⁶⁹T. Nonomura, C. Wen, A. Kato, K. Isobe, Y. Kubota, T. Nakamura, M. Yamashita, Y. Hayakawa, and H. Tatsuoka, *Phys. Proc.* **11**, 110 (2011).
- ⁷⁰C. Gayner and K. K. Kar, *Prog. Mater. Sci.* **83**, 330 (2016).
- ⁷¹Y. F. Liu, R. J. Ma, Y. P. He, M. X. Gao, and H. G. Pan, *Adv. Funct. Mater.* **24**, 3944 (2014).
- ⁷²G. A. Roberts, E. J. Cairns, and J. A. Reimer, *J. Electrochem. Soc.* **151**, A493 (2004).
- ⁷³G. J. Miller, M. W. Schmidt, F. Wang, and T. S. You, "Quantitative advances in the Zintl-Klemm formalism, in Zintl phases," in *Structure and Bonding*, edited by T. Fässler (Springer, Berlin, 2011), Vol. 139.
- ⁷⁴B. Eisenmann, H. Jordan, and H. Schäfer, *Z. Naturforsch. B* **37**, 1564 (1982).
- ⁷⁵S. F. Liu and J. D. Corbett, *J. Solid State Chem.* **179**, 830 (2006).
- ⁷⁶L. L. Wang, A. Kaminski, P. C. Canfield, and D. D. Johnson, *J. Phys. Chem. C* **122**, 705 (2018).
- ⁷⁷B. Eisenmann and H. Schäfer, *Angew. Chem. Int. Ed.* **19**, 490 (1980).
- ⁷⁸B. Eisenmann, H. Jordan, and H. Schäfer, *Z. Naturforsch. B* **39**, 864 (1984).
- ⁷⁹H. G. von Schnering, U. Bolle, J. Curda, K. Peters, W. Carrillo-Cabrera, M. Somer, M. Schultheiss, and U. Wedig, *Angew. Chem. Int. Ed.* **35**, 984 (1996).
- ⁸⁰X. A. Chen, H. Wada, A. Sato, and H. Nozaki, *J. Alloys Compd.* **290**, 91 (1999).
- ⁸¹E. I. Gladyshevskii and R. V. Skolozdra, *Zh. Neorg. Khim.* **9**, 2411 (1964).
- ⁸²H. G. von Schnering and G. Menge, *J. Solid State Chem.* **28**, 13 (1979).
- ⁸³W. F. Kuhs, R. Nitsche, and K. Scheunemann, *Mater. Res. Bull.* **14**, 241 (1979).
- ⁸⁴T. Wadsten, *Acta Chem. Scand.* **21**, 593 (1967).
- ⁸⁵K. E. Woo, J. A. Dolyniuk, and K. Kovnir, *Inorg. Chem.* **58**, 4997 (2019).
- ⁸⁶H. G. von Schnering, M. Schwarz, and R. Nesper, *J. Less Common Metals* **137**, 297 (1988).
- ⁸⁷M. Schwall and B. Balke, *Materials* **11**, 649 (2018).
- ⁸⁸P. Gorai, A. Goyal, E. S. Toberer, and V. Stevanovic, *J. Mater. Chem. A* **7**, 19385 (2019).